

# Optical coherence tomography system mass-producible on a silicon photonic chip

Simon Schneider,<sup>1,\*</sup> Matthias Lauermaun,<sup>1</sup> Philipp-Immanuel Dietrich,<sup>1,2</sup> Claudius Weimann,<sup>1</sup> Wolfgang Freude,<sup>1,2</sup> and Christian Koos<sup>1,2,3</sup>

<sup>1</sup>Institute of Photonics and Quantum Electronics (IPQ), Karlsruhe Institute of Technology (KIT), Engesserstr. 5, 76131 Karlsruhe, Germany

<sup>2</sup>Institute of Microstructure Technology (IMT), Karlsruhe Institute of Technology (KIT), Hermann-von-Helmholtz-Platz 1, 76344 Eggenstein-Leopoldshafen, Germany

<sup>3</sup>christian.koos@kit.edu

\*simon.schneider@kit.edu

**Abstract:** Miniaturized integrated optical coherence tomography (OCT) systems have the potential to unlock a wide range of both medical and industrial applications. This applies in particular to multi-channel OCT schemes, where scalability and low cost per channel are important, to endoscopic implementations with stringent size demands, and to mechanically robust units for industrial applications. We demonstrate that fully integrated OCT systems can be realized using the state-of-the-art silicon photonic device portfolio. We present two different implementations integrated on a silicon-on-insulator (SOI) photonic chip, one with an integrated reference path (OCT<sub>int</sub>) for imaging objects in distances of 5 mm to 10 mm from the chip edge, and another one with an external reference path (OCT<sub>ext</sub>) for use with conventional scan heads. Both OCT systems use integrated photodiodes and an external swept-frequency source. In our proof-of-concept experiments, we achieve a sensitivity of -64 dB (-53 dB for OCT<sub>int</sub>) and a dynamic range of 60 dB (53 dB for OCT<sub>int</sub>). The viability of the concept is demonstrated by imaging of biological and technical objects.

©2016 Optical Society of America

**OCIS codes:** (110.4500) Optical coherence tomography; (250.5300) Photonic integrated circuits; (130.6010) Sensors; (110.4280) Noise in imaging systems; (110.6895) Three-dimensional lithography.

---

## References and links

1. D. Huang, E. A. Swanson, C. P. Lin, J. S. Schuman, W. G. Stinson, W. Chang, M. R. Hee, T. Flotte, K. Gregory, C. A. Puliafito, and J. G. Fujimoto, "Optical coherence tomography," *Science* **254**(5035), 1178–1181 (1991).
2. S. R. Chinn, E. A. Swanson, and J. G. Fujimoto, "Optical coherence tomography using a frequency-tunable optical source," *Opt. Lett.* **22**(5), 340–342 (1997).
3. P. E. Stanga, A. Sala-Puigdollers, S. Caputo, H. Jaberansari, M. Cien, J. Gray, Y. D'Souza, S. J. Charles, S. Biswas, D. B. Henson, and D. McLeod, "In vivo imaging of cortical vitreous using 1050-nm swept-source deep range imaging optical coherence tomography," *Am. J. Ophthalmol.* **157**(2), 397–404 (2014).
4. S. Schneider, A. Krämer, F. Eppler, H. Alemye, C. Huebner, I. Mikonsaari, J. Leuthold, W. Freude, and C. Koos, "Polarization-sensitive optical coherence tomography for characterization of size and shape of nano-particles," in *CLEO: Science and Innovations* (2013), paper AF1J.4.
5. K. Wiesauer, M. Pircher, E. Goetzinger, C. K. Hitzenberger, R. Engelke, G. Ahrens, G. Gruetzner, and D. Stifter, "Transversal ultrahigh-resolution polarization-sensitive optical coherence tomography for strain mapping in materials," *Opt. Express* **14**(13), 5945–5953 (2006).
6. M. Hochberg, N. C. Harris, R. Ding, Y. Zhang, A. Novack, Z. Xuan, and T. Baehr-Jones, "Silicon photonics: the next fabless semiconductor industry," *IEEE Solid-State Circuits Mag.* **5**(1), 48–58 (2013).
7. S. Schneider, M. Lauermaun, C. Weimann, W. Freude, and C. Koos, "Silicon photonic optical coherence tomography system," in *CLEO: Applications and Technology* (OSA, 2014), paper ATu2P.4.
8. G. Yurtsever, N. Weiss, J. Kalkman, T. G. van Leeuwen, and R. Baets, "Ultra-compact silicon photonic integrated interferometer for swept-source optical coherence tomography," *Opt. Lett.* **39**(17), 5228–5231 (2014).
9. Z. Wang, H.-C. Lee, D. Vermeulen, L. Chen, T. Nielsen, S. Y. Park, A. Ghaemi, E. Swanson, C. Doerr, and J. Fujimoto, "Silicon photonic integrated circuit swept-source optical coherence tomography receiver with dual polarization, dual balanced, in-phase and quadrature detection," *Biomed. Opt. Express* **6**(7), 2562–2574 (2015).

10. V. D. Nguyen, N. Weiss, W. Beeker, M. Hoekman, A. Leinse, R. G. Heideman, T. G. van Leeuwen, and J. Kalkman, "Integrated-optics-based swept-source optical coherence tomography," *Opt. Lett.* **37**(23), 4820–4822 (2012).
11. B. I. Akca, D. van Nguyen, J. Kalkman, N. Ismail, G. Sengo, F. Sun, A. Driessen, T. G. van Leeuwen, M. Pollnau, K. Wörhoff, and R. M. de Ridder, "Toward Spectral-Domain Optical Coherence Tomography on a Chip," *IEEE J. Sel. Top. Quantum Electron.* **18**(3), 1223–1233 (2012).
12. B. I. Akca, B. Považay, A. Alex, K. Wörhoff, R. M. de Ridder, W. Drexler, and M. Pollnau, "Miniature spectrometer and beam splitter for an optical coherence tomography on a silicon chip," *Opt. Express* **21**(14), 16648–16656 (2013).
13. S. Yun, G. Tearney, J. de Boer, N. Iftimia, and B. Bouma, "High-speed optical frequency-domain imaging," *Opt. Express* **11**(22), 2953–2963 (2003).
14. T. Baehr-Jones, R. Ding, A. Ayazi, T. Pinguet, M. Streshinsky, N. Harris, J. Li, L. He, M. Gould, Y. Zhang, A. Eu-Jin Lim, T.-Y. Liow, S. Hwee-Gee Teo, G.-Q. Lo, and M. Hochberg, "A 25 Gb/s silicon photonics platform," *ArXiv e-prints*, 1203.0767 (2012).
15. N. Lindenmann, S. Dottermusch, M. L. Goedecke, T. Hoose, M. R. Billah, T. P. Onanuga, A. Hofmann, W. Freude, and C. Koos, "Connecting silicon photonic circuits to multicore fibers by photonic wire bonding," *J. Lightwave Technol.* **33**(4), 755–760 (2015).
16. K. Petermann, *Laser Diode Modulation and Noise* (Kluwer Academic Publishers; KTK Scientific Publishers, 1988).
17. A. M. Rollins and J. A. Izatt, "Optimal interferometer designs for optical coherence tomography," *Opt. Lett.* **24**(21), 1484–1486 (1999).
18. F. Morichetti, A. Canciamilla, C. Ferrari, M. Torregiani, A. Melloni, and M. Martinelli, "Roughness induced backscattering in optical silicon waveguides," *Phys. Rev. Lett.* **104**(3), 033902 (2010).
19. G. Kurczveil, P. Pintus, M. J. R. Heck, J. D. Peters, and J. E. Bowers, "Characterization of Insertion Loss and Back Reflection in Passive Hybrid Silicon Tapers," *IEEE Photonics J.* **5**(2), 6600410 (2013).
20. Y. Yasuno, V. D. Madjarova, S. Makita, M. Akiba, A. Morosawa, C. Chong, T. Sakai, K.-P. Chan, M. Itoh, and T. Yatagai, "Three-dimensional and high-speed swept-source optical coherence tomography for in vivo investigation of human anterior eye segments," *Opt. Express* **13**(26), 10652–10664 (2005).
21. Z. Chen, T. E. Milner, D. Dave, and J. S. Nelson, "Optical Doppler tomographic imaging of fluid flow velocity in highly scattering media," *Opt. Lett.* **22**(1), 64–66 (1997).
22. B. F. Kennedy, K. M. Kennedy, and D. D. Sampson, "A review of optical coherence elastography: fundamentals, techniques and prospects," *IEEE J. Sel. Top. Quantum Electron.* **20**(2), 272–288 (2014).
23. J. Heo, E. Jang, S. Haam, S. J. Oh, Y.-M. Huh, J.-S. Suh, E. Chung, and C. Joo, "In vivo photothermal optical coherence tomography of targeted mouse brain tumors using gold nanostars," in *CLEO: Science and Innovations*, pp. SM4P.3.
24. M. Bonesi, M. P. Minneman, J. Ensher, B. Zabihiyan, H. Sattmann, P. Boschert, E. Hoover, R. A. Leitgeb, M. Crawford, and W. Drexler, "Akinetic all-semiconductor programmable swept-source at 1550 nm and 1310 nm with centimeters coherence length," *Opt. Express* **22**(3), 2632–2655 (2014).
25. H. Peng, A. Bria, Z. Zhou, G. Iannello, and F. Long, "Extensible visualization and analysis for multidimensional images using Vaa3D," *Nat. Protoc.* **9**(1), 193–208 (2014).
26. H. Peng, Z. Ruan, F. Long, J. H. Simpson, and E. W. Myers, "V3D enables real-time 3D visualization and quantitative analysis of large-scale biological image data sets," *Nat. Biotechnol.* **28**(4), 348–353 (2010).
27. H. Peng, J. Tang, H. Xiao, A. Bria, J. Zhou, V. Butler, Z. Zhou, P. T. Gonzalez-Bellido, S. W. Oh, J. Chen, A. Mitra, R. W. Tsien, H. Zeng, G. A. Ascoli, G. Iannello, M. Hawrylycz, E. Myers, and F. Long, "Virtual finger boosts three-dimensional imaging and microsurgery as well as terabyte volume image visualization and analysis," *Nat. Commun.* **5**, 4342 (2014).

## 1. Introduction

Optical coherence tomography (OCT) [1,2] looks back on great advances in the past decades. Micrometer-range resolution in volumetric imaging opened a wide field of applications reaching from ophthalmology in medical diagnostics [3] to particle and defect characterization in materials science [4,5]. While current OCT systems are still assembled from discrete components, optical integration offers the prospect of compact low-cost mass-producible implementations. Especially in endoscopic applications as well as in industrial surface and distance metrology, integrated systems can comply with the demands in size, mechanical robustness, temperature stability and cost. An arrangement of multiple parallel OCT systems becomes feasible, allowing the simultaneous recording of depth scans at different positions (B-scan). Silicon photonics is a particularly attractive platform for integration of OCT systems, lending itself to large-scale photonic-electronic integration on the basis of mature high-yield CMOS processes that are offered by widely available foundry services [6]. Early in 2014, we introduced the first integrated silicon-photonic OCT system with surface imaging capabilities, comprising the interferometer and on-chip photodetectors [7]. In the same year, Yurtsever *et al.* demonstrated a silicon-photonic OCT system and

showed a sensitivity of  $-62$  dB, yet with off-chip photodetectors [8]. Recently, a silicon photonic optical combiner with integrated photodiodes was used as a polarization-diverse receiver for a fiber-based swept-source OCT system [9]. However, for completing the OCT interferometer, external couplers and circulators are used. Other realizations of integrated OCT systems rely on silicon nitride and silicon oxynitride waveguides, where both swept-source [10] and spectral-domain implementations have been shown. These demonstrations comprise, e.g., spectral-domain OCT chips based on arrayed waveguide gratings (AWG) [11], which have been used for characterization of biological samples [12]. Yet, silicon nitride and silicon oxynitride integration platforms are limited to passive components only such as waveguides and power splitters, and hence must be always complemented by external photodetectors. This limits the potential for large-scale integration.

In this paper we demonstrate the first fully integrated silicon photonic OCT system, where receiver and interferometer components are monolithically integrated on a single chip, and where only the swept laser source (SS) and optional fiber-based delay lines are external to the chip. The experiments build upon the state-of-the-art silicon photonic device portfolio and demonstrate the advantages in size, cost and robustness inherent in monolithic integration. Based on our recent results [7] we investigate two system concepts, one with a fixed internal integrated reference path (OCT<sub>int</sub>), and one with external reference path with variable length (OCT<sub>ext</sub>). With the compact OCT<sub>int</sub> system, a lens at the chip edge focuses the swept-source light to the sample and collects the backscattered radiation. The OCT<sub>ext</sub> system allows the use of a conventional OCT scan head positioned remote from the chip. We achieve sensitivities down to  $-64$  dB ( $-53$  dB for OCT<sub>int</sub>) and demonstrate imaging of both technical and biological samples. The sensitivities of our current OCT implementations are limited by relative intensity noise (RIN) and on-chip backscatter. Further improvement is possible by using optimized integrated components and by reducing reflections at the chip edges. Each of the OCT circuits occupies an on-chip area of less than  $0.4$  mm<sup>2</sup>.

This paper is organized as follows: In Sect. 2 we introduce the concept and the implementation of the OCT<sub>int</sub> and OCT<sub>ext</sub> systems. In Sect. 3 we discuss the sensitivity and the dynamic range of the systems. Sect. 4 is dedicated to the evaluation of the performance of both systems by demonstrating two-dimensional and three-dimensional imaging of technical and biological samples. A summary and an outlook are given in Sect. 5 and conclude the paper.

## 2. Silicon photonic OCT systems and experimental setup

Both the OCT<sub>int</sub> and OCT<sub>ext</sub> systems use the principle of swept-source OCT [2]. In general, an OCT system measures the position and the strength of a multitude of scatterers along a light path in a sample at various distances  $z - z_0$  from a reference plane at  $z_0$ . To this end, the electric field  $E_S$  that is backscattered from a sample is compared in amplitude and phase to a reference field  $E_R$ . Both the sample and the reference field are derived from the same external optical swept-wavelength source. In an interferometer arrangement, sample and reference fields are superimposed on a (balanced) photodetector, the output current of which contains patterns resulting from interference of the backscattered field with the reference field. From these patterns, the amplitude and the position  $z - z_0$  of the backscatter along the light path can be obtained by Fourier analysis of the photocurrent [2]. The backscatter strength denotes the ratio of backscattered optical power to optical power incident on the sample. For an optimum sensitivity, the optical length difference between the return path from the sample and the reference path should be small compared to the coherence length  $l_c$  of the source [13].

The integrated OCT configurations presented in this work are depicted in Fig. 1 and Fig. 2 and are described in more detail in the subsequent sections. In each of the implementations, the photonic integrated circuits (PIC) comprise passive waveguides and 3-dB couplers (CPL) based on multimode interference (MMI), forming an interferometer structure which is connected to on-chip germanium photodiodes (PD). Silicon photonics allows for particularly compact implementations: Both OCT systems were co-integrated on the same chip along with a large number of further optical circuits for various applications – the on-chip area occupied

by each of the OCT circuits is less than  $0.4 \text{ mm}^2$ , and is dominated by the contact pads of the photodetectors which could be further reduced in size. As an external light source, we use a commercially available swept-source laser (Santec HSL-2100-ST) featuring a center wavelength of 1315 nm and a scanning range of 110 nm. The source is coupled to the PIC by either a lensed fiber (LF) or a polymer microlens (PL). All waveguides leading to chip facets are equipped with tapers narrowing towards the facet, designed for the full width at half maximum (FWHM) spot size of  $1.9 \text{ }\mu\text{m}$  of the lensed fibers. An external polarization controller (PoC) is used to precisely excite the quasi-TE mode of the on-chip waveguides. The interference signal is recorded by two balanced on-chip photodiodes, which are specified to have a bandwidth of 20 GHz. The electrical signal from the photodiodes is tapped by an RF probe, combined for balanced detection, subsequently amplified, recorded by an analog-to-digital converter, and further processed on a computer. While the OCT<sub>int</sub> system as described in Sect. 2.1 has the reference path integrated on-chip and thus allows for measuring samples directly in front of the chip edge, the OCT<sub>ext</sub> system as described in Sect. 2.2 has an external reference path and allows imaging with a standard OCT scan head, meters away from the chip. Both PIC were fabricated on a silicon-on-insulator (SOI) wafer with a  $2 \text{ }\mu\text{m}$  thick buried oxide and a 220 nm thick device layer using 248 nm lithography in the framework of a standard multi-project-wafer (MPW) run. For fabrication, the *OpSIS* service was made use of through *IME A\*STAR* in Singapore, using design elements from the *OpSIS OI25A* PDK [14].

### 2.1 OCT chip with internal integrated reference path (OCT<sub>int</sub> system)

The experimental setup and the silicon photonic integrated circuit (PIC) of the OCT<sub>int</sub> system are shown in Fig. 1(a). The reference path (RP) of the OCT interferometer is integrated on the chip. The length of the reference path is designed such that the reference position  $z_0$  of the depth scan coincides with the output facet of the PIC, i.e., sample and reference light interfering at the power combiner CPL2 have traveled the same distance through integrated on-chip transport waveguides. All transport waveguides are uniform and the associated modes feature identical effective refractive indices which are invariant along the propagation direction. This leads to inherent compensation of dispersion in the on-chip sections of the reference and the sample path. The swept-source laser has +11 dBm (12.6 mW) of output power and is edge-coupled to the PIC by a lensed fiber having a  $1.9 \text{ }\mu\text{m}$  FWHM-spot size diameter, matched to the spot size of the waveguide tapers. This leads to an attenuation of 5 dB at the input facet and to an on-chip power of approximately +6 dBm (4 mW), averaged over a 100 nm wavelength span from 1270 nm to 1370 nm. A polarization controller (PoC) aligns the polarization according to the quasi-TE mode of the chip waveguides. In the sample path, a silica ball lens (BL) with a diameter of 1 mm is used to focus the radiation emerging from the chip facet and to collect the backscattered light from the sample. Figure 1(b) shows a micrograph of the PIC along with the lensed fiber, the ball lens and the RF probe.

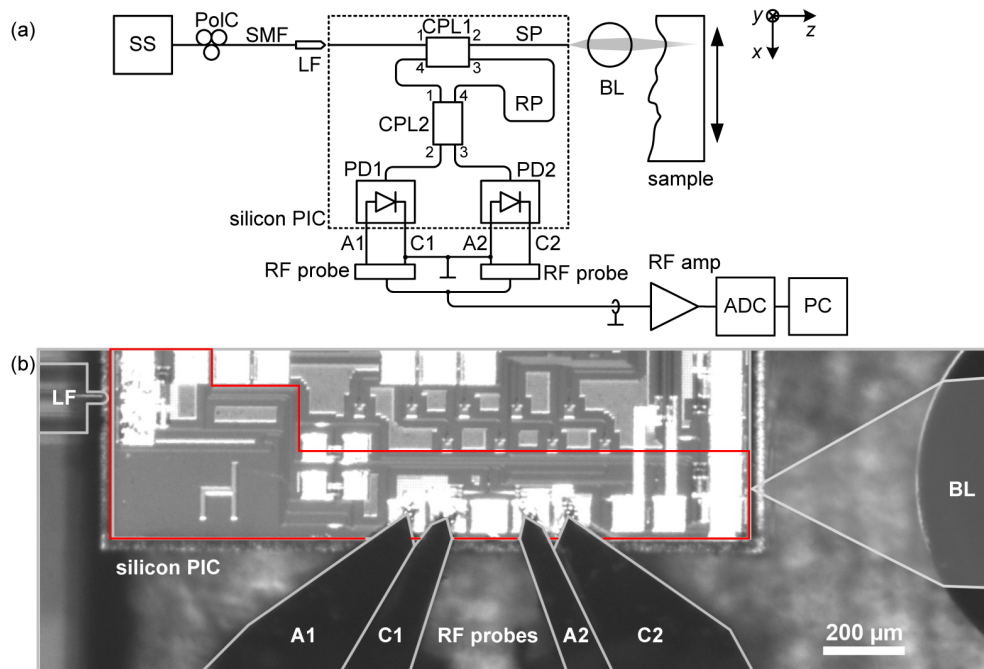


Fig. 1. OCT<sub>int</sub> system configuration with integrated reference path: Experimental setup and photonic integrated circuit (PIC). (a) Schematic of setup. SS: swept-source laser, PoLC: polarization controller, LF: lensed fiber, CPL1,2: 3 dB couplers with ports designated by 1...4, BL: ball lens, SP: sample path, RP: reference path, PD1,2: photodiodes with anodes (A1,2) and cathodes (C1,2), RF amp: RF amplifier, ADC: analog-to-digital converter, PC: personal computer. The photodiodes are contacted with RF probes and their photocurrents are subtracted for balanced detection. (b) PIC microscope image with optical input (LF), optical port with free-space path (via BL) to and from the sample, along with electrical connections (via RF probes). The OCT<sub>int</sub> system was co-integrated with a large number of additional optical circuits used for other purposes – the occupied on-chip area is indicated by a red frame and amounts to less than 0.4 mm<sup>2</sup>.

## 2.2 OCT chip with external reference path (OCT<sub>ext</sub> system)

The experimental setup and the silicon photonic integrated circuit (PIC) of the OCT<sub>ext</sub> configuration with external reference path are depicted in Fig. 2(a). In contrast to the OCT<sub>int</sub> structure in Fig. 1, the reference path (RP) is routed out of and fed back into the chip. The external reference path with adjustable length allows a long sample path (SP) and the use of a conventional scan head consisting of a fiber-collimator (FC) with angled physical contact connector (APC), a pair of galvo scan mirrors and an OCT scan lens. The reference path comprises a free-space section for precise length adjustments. Polarization controllers (PoLC) align the polarization according to the quasi-TE mode of the chip waveguides. Efficient fiber-chip coupling is enabled by a novel kind of microlenses that can be fabricated in situ by using direct-write three-dimensional laser lithography [15]. Figure 2(b) shows a microscope image of the chip facet with attached polymer lenses. Fiber-chip coupling loss was estimated by a combination of transmission and photocurrent measurements. The lensed ports on the right-hand side couple to standard single-mode fibers (SMF) with typical losses of 4 dB (6 dB at maximum) over a 100 nm wavelength span from 1270 nm to 1370 nm. The lensed port at the left-hand side has a loss between 7 dB and 10 dB in the same wavelength range, due to an offset error between lens center and chip waveguide. With this coupling scheme and an available laser source power of +11 dBm (12.6 mW), we estimate a wavelength-averaged on-chip power of +3 dBm (2 mW). The average power incident on the sample was measured to

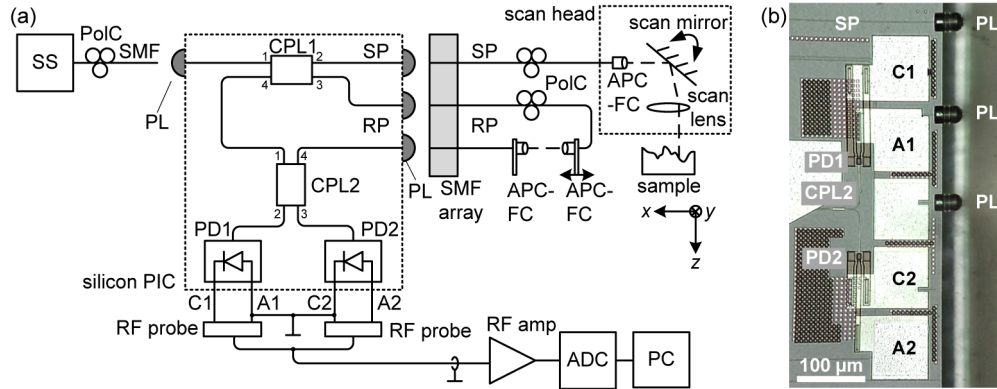


Fig. 2. OCText configuration with long external reference and sample paths: Experimental setup and photonic integrated circuit (PIC). (a) Schematic of setup. SS: swept-source laser, PoC: polarization controller, SMF: single-mode fiber, PL: polymer lens, CPL1,2: 3 dB couplers with ports designated by 1...4, SP: sample path, RP: reference path, PD1,2: photodiodes with anodes (A1,2) and cathodes (C1,2), APC-FC: fiber collimator (FC) with angled physical contact connector (APC), RF amp: RF amplifier, ADC: analog-to-digital converter, PC: personal computer. The photodiodes are contacted with RF probes and their photocurrents are subtracted for balanced detection. (b) PIC microscope image of the chip's right edge. The OCText system is co-integrated with a large number of additional optical circuits used for other purposes – the occupied on-chip area amounts to less than  $0.4 \text{ mm}^2$ . SP: silicon waveguide for sample path, C1,2 and A1,2: contact pads for photodiode readout with RF probes, PL: Three polymer lenses between chip waveguides and a standard single-mode fiber array.

be  $-5 \text{ dBm}$  ( $0.3 \text{ mW}$ ), and the average reference path power received by each of the photodiodes is estimated to be  $-17 \text{ dBm}$  ( $20 \text{ } \mu\text{W}$ ).

### 3. Sensitivity and dynamic range

Noise and parasitic backscatter limit both the sensitivity and the dynamic range (DR) of the system. The sensitivity is defined as the minimum measurable sample reflectivity, which is determined by the noise level of the system. The dynamic range, in turn, denotes the maximum achievable signal-to-noise power ratio (SNR) and is smaller than or equal to the sensitivity. In our implementations, noise is dominated by either the relative intensity noise (RIN) of the swept source or by parasitic backscatter – thermal noise of the photodiode RF amplifier is irrelevant in all cases.

Figure 3 illustrates the different signal and noise contributions as applicable to the two OCT systems. In general, the relative intensity noise of a laser source relates the variance of the optical power fluctuations to the mean power squared [16]. The relative intensity noise is generally described by its single-sided power spectrum  $\text{RIN}(f - f_c)$  centered at the carrier frequency  $f_c$ , and can be obtained from a spectral analysis of the photocurrent in the baseband. The spectrum  $\text{RIN}(f - f_c)$  is specified in units of  $\text{Hz}^{-1}$ , or, in logarithmic form, as  $\text{dB Hz}^{-1}$ . The total RIN results from an integration over all frequencies,

$$\text{RIN}_{\text{tot}} = \int_0^{\infty} \text{RIN}(f - f_c) df, \quad (1)$$

$$\text{RIN}_{\text{dB}}(f - f_c) = 10 \lg(\text{RIN}(f - f_c) \times 1 \text{ Hz}) \quad (\text{in dB Hz}^{-1}).$$

In swept-source OCT, balanced detection is normally used. The photocurrent then only exhibits RIN contributions that result from the interference of the sample field and the reference field, whereas the individual RIN fluctuations of the sample and the reference signal

cancel if ideal balancing is assumed [17]. As a consequence, a reflection peak at  $z = z_c$  is surrounded by an accompanying noise profile  $\text{RIN}_z(z - z_c)$ . Assuming an idealized SS laser for which the optical frequency increases linearly with time, the depth offset  $z - z_c$  from the reflection peak is proportional to a baseband frequency offset, which in these experiments is  $f - f_c = (z - z_c) \times 3.55 \text{ MHz/mm}$ . This value was determined by inserting a mirror into the sample path and by measuring the frequency shift of the photocurrent spectrum in MHz as a function of mirror position in mm. Using the relation  $\text{RIN}_z(z - z_c) = \text{RIN}(f) \times df/dz$ , the spatial relative intensity noise profile is then given by

$$\text{RIN}_z(z - z_c) = \text{RIN}((z - z_c) \times 3.55 \text{ MHz/mm}) \times 3.55 \text{ MHz/mm}. \quad (2)$$

When expressed in logarithmic form, it is convenient to consider the RIN contribution within a spatial element that corresponds to the depth resolution of  $\delta z = 8 \mu\text{m}$  of the OCT system in vacuum,

$$\text{RIN}_{z,\text{dB}}(z - z_c) = 10 \lg(\text{RIN}_z(z - z_c) \times 8 \mu\text{m}) \quad (\text{in dB}(8 \mu\text{m})^{-1}). \quad (3)$$

For a linear sweep of the optical frequency, the depth resolution of  $\delta z = 8 \mu\text{m}$  is equivalent to a  $\delta z \times 3.55 \text{ MHz/mm} = 28.4 \text{ kHz}$  frequency resolution of the photocurrent spectrum. The position-dependent  $\text{RIN}_z(z - z_c)$  of the SS laser can be directly measured using a conventional fiber-based OCT setup, see Fig. 3(a). To this end, a fully reflecting (full refl.) mirror is introduced at position  $z_c - z_0 = 1 \text{ mm}$ , leading to a spatial relative intensity noise profile  $\text{RIN}_{z,\text{dB}}(z - z_c)$  centered at  $z_c - z_0 = 1 \text{ mm}$  (thin blue curve). The thick blue curve provides a schematic of these data for a spatial resolution of  $\delta z = 8 \mu\text{m}$ . In the immediate neighborhood of this reflection peak at  $z_1 - z_c = 0 \text{ mm}$ , we measure  $\text{RIN}_{z,\text{dB}}(0) = -60 \text{ dB}(8 \mu\text{m})^{-1}$ , which is by 60 dB smaller than the reflection peak. Further away from the reflecting mirror, e. g., at  $z_9 - z_c = 8 \text{ mm}$ , we find  $\text{RIN}_{z,\text{dB}}(z_9 - z_c) = -80 \text{ dB}(8 \mu\text{m})^{-1}$ , which is smaller than the reflection peak by 80 dB. If the mirror is replaced by a  $-50 \text{ dB}$  reflector, the noise is about 100 dB down (gray curve), dominated by residual RIN due to non-ideal balancing of the photodetectors. The spurious peaks in the gray curve in Fig. 3(a) stem from weak reflections in the setup. As a comparison, we measure the one-sided relative intensity noise spectrum  $\text{RIN}(f)$  of the Santec swept-laser source with a photodiode and an electrical spectrum analyzer. We find  $\text{RIN}_{\text{dB}}(f_a) = -105 \text{ dB Hz}^{-1} = -60 \text{ dB}(28.4 \text{ kHz})^{-1}$  for  $f_a = 3.55 \text{ MHz}$ , which corresponds to  $\text{RIN}_{z,\text{dB}}(z_a - z_1) = -60 \text{ dB}(8 \mu\text{m})^{-1}$  at a distance of  $z_a - z_1 = 1 \text{ mm}$  from the peak of a fully reflecting mirror, in perfect agreement with the results obtained from the OCT measurement. Similarly, at a larger baseband frequency  $f_b = 30 \text{ MHz}$ , we measure  $\text{RIN}_{\text{dB}}(f_b) = -125 \text{ dB Hz}^{-1} = -80 \text{ dB}(28.4 \text{ kHz})^{-1}$ , corresponding to  $\text{RIN}_{z,\text{dB}}(z_b - z_1) = -80 \text{ dB}(8 \mu\text{m})^{-1}$  at a distance of  $z_b - z_1 = 8.5 \text{ mm}$  from the peak. These numbers are similar to RIN figures reported for other swept-source lasers [13].

Besides RIN, distributed on-chip backscatter can be a reason for sensitivity limitations of integrated OCT systems. On-chip backscatter is mainly caused by random sidewall roughness or other irregularities of high index-contrast waveguides, which couple forward and backward-propagating fundamental modes to each other [18]. Interference of the backscattered light with the reference light or with light from spurious reflections on the PIC leads to a continuous measurement background. This unwanted interference signal may be suppressed by the common-mode rejection of a balanced detector if both backscattered light and reference light are coupled to the same input port of the combiner CPL2 in front of the

balanced detector. Coherent backscatter is hence only visible in case of imperfect common-mode rejection or if backscattered light and reference light are coupled to different input ports of the combiner.

**OCT<sub>int</sub>** In case of the OCT<sub>int</sub> system, Fig. 1 and Fig. 3(b), the chip edge reflection at  $z_{\text{edge,int}} - z_0 = 0$  mm amounts to around 3% (−15 dB) and is by 24 dB larger than the light returned via free-space propagating from a fully reflecting (full refl., return loss 0 dB) plane mirror. This corresponds to single-pass coupling losses between the chip and the free-space beam of approximately 20 dB. Since the depth information in SS-OCT results from a Fourier analysis of the real-valued time-domain data, negative depths cannot be discriminated from the true positive depths (depth degeneracy). Therefore the on-chip backscatter appears also at depths  $z - z_0 > 0$ . In the OCT<sub>int</sub> system, distributed on-chip backscatter (black) dominates over the RIN associated with the strong reflection from the chip edge for small depths  $z - z_0 < 5$  mm, corresponding to the optical path lengths of the on-chip waveguides. For bigger depths  $z - z_0 > 5$  mm, the influence of on-chip backscatter can be neglected, and the sensitivity is limited by the RIN background (blue) caused by the chip edge peak. This RIN background is  $\text{RIN}_{z,\text{dB}}(z_8 - z_0) = -80 \text{ dB} (8 \mu\text{m})^{-1}$  below the maximum of the chip edge peak, leading to a sensitivity of −56 dB. The total background consists of the sum of on-chip backscatter and RIN (amber dotted line). Since relative intensity noise originating from the chip edge dominates all noise contributions that could possibly come from other objects (red: full refl.; green: low refl.), the DR is 56 dB.

For the OCT<sub>int</sub> system, sensitivity can be drastically improved by reducing the chip edge reflections using, e.g., angled chip facets [19], or by improving coupling efficiency to and from the chip, using, e.g., polymer microlenses as for the OCT<sub>ext</sub> system. Assuming a reduction of facet reflectivity to below −30 dB and a reduction of the single-pass coupling losses to less than 5 dB, as in the OCT<sub>ext</sub> system, we believe that sensitivity improvements of approximately 45 dB can be achieved.

**OCT<sub>ext</sub>** The situation is different in the case of the OCT<sub>ext</sub> system, Fig. 2 and Fig. 3(c), where the chip edge peak at  $z_{\text{edge,ext}}$  is far outside the source coherence window (long reference path,  $z_{\text{edge,ext}} - z_0 = -8$  m). The associated  $\text{RIN}_z(z_1 - z_{\text{edge,ext}})$  in the measurement window near  $z_1 - z_0 = 1$  mm corresponds to  $\text{RIN}(28.4 \text{ GHz})$ , which is many orders of magnitude smaller than the RIN levels measured at MHz frequencies as described above. For the OCT<sub>ext</sub> system, RIN from the chip edge reflection can hence be safely neglected as a relevant source of signal impairment. Moreover, on-chip backscatter (black) is less prominent for the OCT<sub>ext</sub> system than for the OCT<sub>int</sub> system. Due to the long fiber-based RP and the limited coherence length of the source, on-chip backscatter does not coherently interfere with the reference light. For a perfectly balanced pair of photodiodes, on-chip backscatter should hence not be visible at all. This is different for the more realistic case of imperfect balancing, where the photocurrent may also contain signal components that result from interference of optical signals that are coupled to the same port of CPL2 of the OCT<sub>ext</sub> system. In this case, spurious reflections at the chip edges or at CPL 1 may act as a parasitic reference signal and generate an interference signal with distributed on-chip backscatter, thus limiting the sensitivity. In our implementation, the parasitic reference signal is dominated by light reflected at the chip edges of both SP and RP.

To obtain an estimate of the signal background associated with on-chip backscatter, we perform an independent measurement to determine the overall on-chip backscatter of the SP and RP waveguides to approximately  $\rho_{\text{WG,dB}} = -50 \text{ dB}$  within the depth resolution of 8  $\mu\text{m}$ . To translate this into a signal background in the OCT measurement, we need to estimate the strength of the parasitic reference signal. To his end, the chip edge reflection of each of the SP

and RP waveguide ports is assumed to amount to  $-15$  dB (3%) as in the case of the *OCTint* system, and the on-chip input power is estimated to  $+3$  dBm (2 mW). Taking into account 1 dB of excess loss for each of CPL1 and CPL2, the parasitic reference light coupled to each of the photodiodes thus amounts to  $-21$  dBm ( $8 \mu\text{W}$ ), which is  $\delta_{\text{dB}} = 4$  dB less than the reference light from the off-chip reference path. Moreover, the parasitic reference light and the on-chip backscatter are coupled through the same port 1 to CPL2, and their interference signal is therefore attenuated by the common-mode rejection ratio (CMRR) of the balanced receiver, which amounts to  $\zeta_{\text{dB}} = 15$  dB. Taking into account the insertion loss of the lensed ports towards the sample,  $a_{\text{dB}} = 4$  dB, and referring the backscatter to an ideal mirror in the off-chip sample path, the backscatter floor in the OCT measurement can be estimated to be  $\rho_{\text{BG,dB}} = \rho_{\text{WG,dB}} + 2a_{\text{dB}} - \delta_{\text{dB}} - \zeta_{\text{dB}} = -61$  dB. This backscatter floor limits the sensitivity to  $-61$  dB and is the relevant limitation for low sample reflectivities (green: low refl.). For strong reflectivities, the total background consists of the sum of on-chip backscatter and RIN (amber dotted line) associated with the reflection peak. For a fully reflecting mirror (red: full refl.) the associated  $\text{RIN}_{z,\text{dB}}(z_1 - z_0) = -60 \text{ dB} (8 \mu\text{m})^{-1}$  determines the DR of 60 dB.

For the *OCText* system, the sensitivity limitations can be mitigated in various ways: On-chip backscatter can be reduced by optimizing the fabrication processes of the waveguides – our current experiments were based on a standard silicon photonic MPW process for optical communications, where backscatter has not been considered a crucial aspect that requires special attention. Moreover, the chip edge reflections can be reduced to values well below  $-30$  dB, by using, e.g., angled waveguide facets [19], which would lead to lower parasitic reference signals. Additionally, improved balancing of the coupler (CPL2) in front of the balanced detectors leads to an increased CMRR and thus further improves the sensitivity of the *OCText* system. Using more advanced power combiners with tunable splitting ratio, e.g., based on Mach-Zehnder interferometers and phase shifters, we believe that CMRR values of significantly better than 30 dB can be achieved, leading to overall sensitivity improvements of more than 30 dB.

#### 4. Performance evaluation and application demonstration

The performance of the integrated OCT systems was assessed by measuring sensitivity, dynamic range and depth scanning range with a plane mirror as a test object placed at various depth positions  $z - z_0$ . In addition, two- and three-dimensional OCT images of technical and biological samples are taken.

##### 4.1 OCT chip with internal integrated reference path (*OCTint* system)

The *OCTint* system is investigated by using a movable plane mirror as a sample. For calibrating the backscatter measurements, a fully reflecting sample mirror is placed at a position  $z - z_0 = 8$  mm away from the chip edge  $z_{\text{edge,int}} - z_0 = 0$ . Figure 4(a) depicts measured depth scans. For various mirror positions between 5 mm and 12 mm (brightly colored scans) the scans are superimposed, each curve resulting from averaging 100 scans. Because the depth information results from a Fourier analysis of the scan traces in the frequency domain, negative depths  $z - z_0 < 0$  located inside the chip cannot be discriminated from the true positive depths outside the chip (depth degeneracy). Therefore the on-chip backscatter (black part of the scan) appears also in space-inverted form at depths  $z - z_0 > 0$  (gray part of scan), and the backscatter from the mirrors could be also seen at  $z - z_0 < 0$  (lightly colored scans).

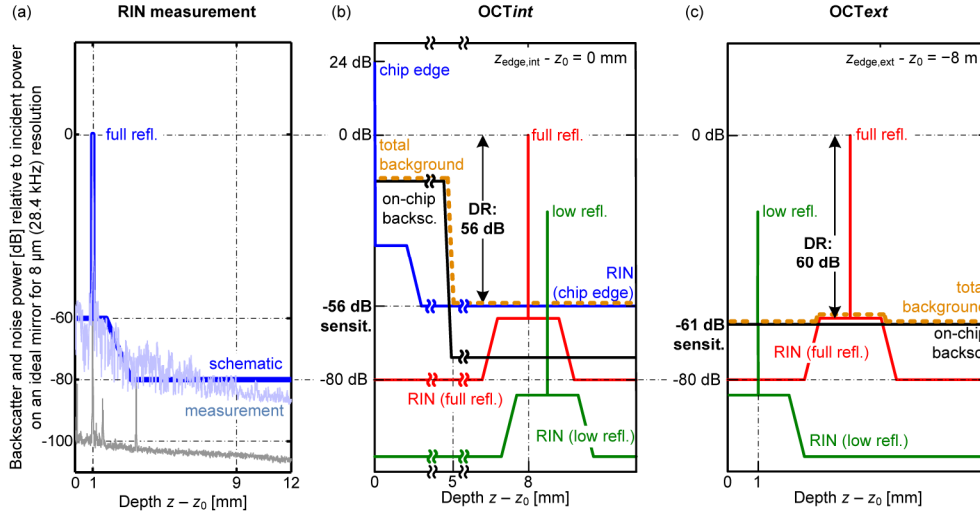


Fig. 3. Sensitivity and dynamic range (DR) derived from a measured OCT scan in a conventional setup, and from A-scan schematics for configurations OCT<sub>int</sub> and OCT<sub>ext</sub>. Horizontal axes: Measurement depth  $z - z_0$  referred to a reference position  $z_0$ . Vertical axes: Backscatter signal and noise power relative to the power reflected from an ideal mirror at position  $z_M$ . All relative intensity noise data are related to the OCT resolution bandwidth of 28.4 kHz, or, equivalently, to the OCT depth resolution of 8 μm. (a) Measurement of RIN background of the swept source used for the OCT<sub>int</sub> and OCT<sub>ext</sub> system: The profile of the RIN<sub>z,dB</sub> background is derived from the measured backscatter signal of a fully reflecting mirror (full refl.) positioned at  $z_1 - z_0 = 1$  mm in a conventional fiber-based OCT setup (thin blue curve: measurement, thick blue curve: schematic approximation). The spatial RIN<sub>z,dB</sub>( $z - z_c$ ) profile for a resolution of 8 μm is about 80 dB down and results from the interference of reflected source RIN with the reference field. If the fully reflecting mirror is replaced by a partially reflecting mirror (power reflection factor -50 dB), the noise level corresponds to a reflectivity of -100 dB (gray curve, spurious peaks originate from weak multiple reflections in the setup), because the balanced receiver suppresses the source RIN, which is transmitted now mainly along the reference path. (b) Noise and backscatter background for the OCT<sub>int</sub> setup. At small distances  $z - z_0 < 5$  mm, on-chip backscatter (on-chip backsc., black) is dominant. At larger distances  $z - z_0 > 5$  mm, RIN from the strong reflection at the chip edge (blue,  $z_{\text{edge,int}} = z_0$ ) dominates the noise level for any sample reflectivity. The total background consists of the sum of on-chip backscatter and RIN (amber dotted line). Both a fully reflecting mirror (full refl., red) and a partially reflecting mirror (low refl., green) lead to similarly shaped, but shifted RIN contributions which are smaller than the RIN related to the chip edge reflection peak. The minimum detectable reflectivity (sensitivity) is -56 dB and represents also the DR of the system. (c) Noise and backscatter background for the OCT<sub>ext</sub> setup with schematic backscatter curves. The chip edge peak at  $z_{\text{edge,ext}} - z_0$  is far outside the source coherence window (long reference path,  $z_{\text{edge,ext}} - z_0 = -8$  m). However, on-chip backscatter (on-chip backsc., black) falls within the coherence window and limits the sensitivity to -61 dB. RIN from a fully reflecting mirror (full refl., red) is responsible for the noise floor 60 dB below the peak. The DR is therefore 60 dB. The total background consists of the sum of on-chip backscatter and RIN (amber dotted line). A weaker mirror reflectivity (low refl., green) can be measured as long as it is larger than -61 dB.

Note that the depth axis was derived assuming light propagation in vacuum, such that internal backscatter appears over a 5 mm long depth range even though the scattering on-chip waveguides are approximately 1.4 mm long. The measurement range is hence limited to  $z - z_0 > 5$  mm. Because the edge reflection cannot be removed, the associated fluctuations due to relative intensity noise determine the noise floor in the measurement window and therefore the sensitivity, as has been explained in Sect. 3 and Fig. 3(b). For mirror positions between 5 mm and 10 mm, the noise level is measured to be between 50 dB and 53 dB below the mirror reflection leading to a dynamic range of up to 53 dB. The minimum measurable sample reflectivity would be -53 dB and defines the measurement sensitivity. This is in good

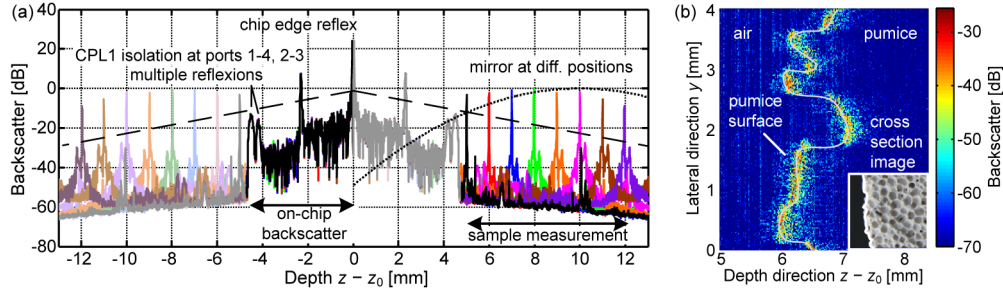


Fig. 4. Backscatter measurements on the OCT<sub>int</sub> chip with integrated reference path. (a) Reflections from a plane mirror at 8 (positive) depth positions  $z - z_0$ . A depth  $z - z_0 = 0$  corresponds to the chip edge. The black broken line is the spatial autocorrelation function of the light source with a 10 dB coherence length of  $l_c = 2 \times 6$  mm in vacuum. The beam is focused by a ball lens (BL) at  $z - z_0 = 10$  mm. The defocusing function (black dotted line) describes the depth-dependent variations of the power reflected from a plane mirror and coupled back into the on-chip waveguide. The drop in spatial coherence (black broken line) partially compensates the defocusing function. The 8 axial A-scans of the mirror backreflections are superimposed (brightly colored scans, normalized to the maximum of the 8 backreflections). The finite isolation of ports 1-4 and 2-3 of coupler CPL1, multiple reflections, and irregularities inside the chip lead to backscatter at negative depths ( $z - z_0 < 0$ , black part of scan). Because the depth information results from a Fourier analysis of the scan traces in the  $k$ -domain, negative depths cannot be discriminated from the true positive depths (depth degeneracy). Therefore the on-chip backscatter appears also at depths  $z - z_0 > 0$  (gray part of scan), and the backscatter from the mirrors could be also seen at  $z - z_0 < 0$  (lightly colored scans). The backscatter in combination with the depth degeneracy limits the measurement range to  $z - z_0 > 5$  mm. The measured mirror reflections are uniform with variations of less than 3 dB for mirror positions between 5 mm and 10 mm. The noise is measured to be between 50 dB and 53 dB below the mirror reflection leading to a dynamic range of up to 53 dB. A minimum measurable sample reflectivity of  $-53$  dB defines the measurement sensitivity. (b) Two-dimensional B-scan of a piece of pumice. The gray line emphasizes the sample surface. The porous surface structure is clearly visible on both the B-scan and the photograph of the cross-section (inset).

agreement with the 56 dB DR and the  $-56$  dB sensitivity estimated for the OCT<sub>int</sub> system in Section 3. The spatial variation of the measured peak reflectivities is attributed to the finite coherence length of the swept source and the finite Rayleigh range of the focused Gaussian beam after the ball lens. The spatial autocorrelation function of the swept-source laser in vacuum is shown as a black broken line in Fig. 4(a). A 10 dB coherence length of  $l_c = 2 \times 6$  mm can be inferred. The drop in measured reflectivities for positions outside the focus is described by a defocusing function, black dotted line in Fig. 4(a). If the ball lens focus is positioned properly, here at 10 mm from the chip facet, the resulting defocusing function partially compensates the signal drop caused by the limited coherence length.

The axial 3 dB-resolution was measured to be  $11 \mu\text{m}$ , which is slightly worse than the  $7 \mu\text{m}$  estimated from the wavelength scanning range of the source. Since dispersion is inherently compensated by equal lengths of on-chip waveguide sections, the reduced resolution is attributed to an imperfect knowledge of the frequency-time relation of the swept-frequency source. In general, the frequency of the tunable laser does not increase linearly with time during the rising slope of a frequency sweep. This can be compensated by digital signal processing if the nonlinearity of the frequency sweep is known exactly. To this end, the time-dependent increase of frequency must be extracted from a calibration measurement using a mirror as sample reflector [20]. Ideally, for a system with no dispersion imbalance between the sample and the reference path, this time-frequency mapping should lead to an axial resolution that is only limited by the tuning range of the swept source. In practice, however,

residual errors of the measured time-dependent increase of frequency lead to a depth-dependent broadening of the reflection peaks in  $z$ -space.

The imaging capability of the OCT<sub>int</sub> system is tested by two-dimensional measurements of a piece of pumice, Fig. 4(b). Strong scattering prevents measurable reflections from deeper ranges inside the material, but the porous surface structure is clearly visible (see the photograph in the inset).

#### 4.2 OCT chip with external reference path (OCT<sub>ext</sub> system)

The OCT<sub>ext</sub> system is also investigated by using a movable plane mirror as a sample. For calibrating the backscatter measurements a sample mirror with a 1% reflection factor (20 dB return loss) is placed at a position  $z - z_0 = 1$  mm within the measurement window  $1 \text{ mm} \leq z - z_0 \leq 10 \text{ mm}$ . The chip edge is located at  $z_{\text{edge, ext}} - z_0 = -8$  m and hence does not influence the measurements. Figure 5(a) shows the superposition of single depth-scans (A-scans) for a single -20 dB sample reflector placed at 1 mm increments within the measurement window. The sample reflector comprises a plane mirror and a neutral density filter with 10 dB single-pass attenuation. Each curve results from averaging 100 scans. The noise level, which defines the sensitivity of the system with respect to a 0 dB reference return loss, is measured to be -64 dB. This is in fair agreement with the sensitivity of -61 dB estimated in Sect. 3 based on an analysis of effects of spurious on-chip backscatter.

The imaging depth of the OCT<sub>ext</sub> system is mainly limited by three effects: The limited coherence length of the source (black broken line), the defocusing of the measurement beam which leads to a drop of power coupled back into the fiber for positions outside the focus (defocusing function, black dotted line), and by residual errors of the time-frequency mapping of the swept source. These residual errors lead to a depth-dependent broadening and a decrease of the maxima of the reflection peaks in  $z$ -space. The total decay caused by limited coherence, defocusing and imperfect time-frequency mapping amounts to approximately 3.3 dB / mm, see Fig. 5(a).

The depth resolution of the system is 30  $\mu\text{m}$ , which is significantly worse than the 7  $\mu\text{m}$  expected from the tuning range of the swept source, also when taking into account the effects of imperfect time-frequency mapping. The rather bad axial resolution is caused by unbalanced dispersion in the sample and reference path. This originates from the fact that the sample and the reference path are composed of different fiber lengths and different path lengths of the on-chip SOI waveguides. Dispersion-induced resolution limitations can be overcome by carefully designing the dispersion maps of the two paths.

Using a perfect reflector, the measured dynamic range is 60 dB at  $z - z_0 = 1$  mm (not shown) and is limited by the laser RIN. This DR agrees very well with the DR of 60 dB estimated in Section 3, see also Fig. 3(c). The dynamic range is not limited by the RIN originating from the reflection at the chip edge, which is located at  $z_{\text{edge, ext}} - z_0 = -8$  m far outside the measurement range. The corresponding RIN (28.4 GHz) is not measurable.

The applicability of the system to sample imaging is demonstrated with 3D volume scans of biological and non-biological samples. Figure 5 shows three-dimensional scans (C-Scans) of a piece of pumice (b), a part of a decayed leaf of cornus sanguinea (c), and a reel of adhesive tape (d).

## 5. Summary and outlook

We demonstrate silicon photonic swept-source OCT systems with integrated photodetectors. We design, implement and characterize two different OCT configurations with on-chip internal reference path (OCT<sub>int</sub>) and with external reference path (OCT<sub>ext</sub>). We demonstrate

the viability of the systems by imaging both technical and biological samples: Configuration OCT<sub>int</sub> enables imaging directly in front of the chip facet. For this system, we measure sensitivities between  $-50$  dB and  $-53$  dB over 5 mm axial scanning range. As a demonstration, we show a cross-sectional B-scan of a scattering pumice sample. Configuration OCT<sub>ext</sub> supports the use of a remote standard OCT scan head. For this system, a sensitivity of  $-64$  dB was achieved – the best value reported so far for a fully integrated optical OCT processing unit. The OCT<sub>ext</sub> system achieves a better sensitivity than the OCT<sub>int</sub> system, although a larger number of fiber-chip interfaces add to the coupling loss. However, our directly written [15] optimized polymer microlenses minimize this loss. For the

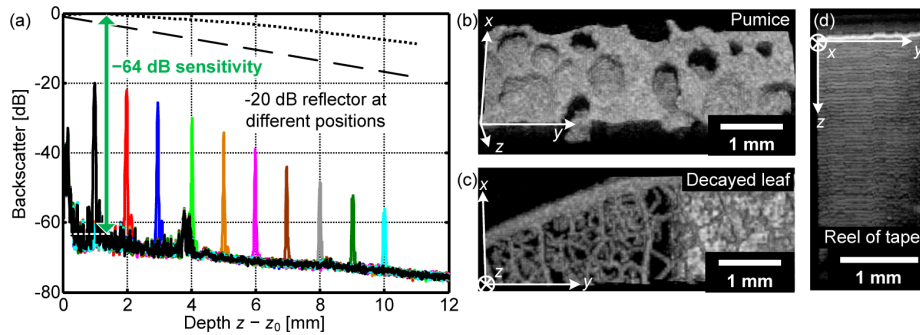


Fig. 5. Backscatter measurements obtained with the OCT<sub>ext</sub> chip using an external reference path. A depth  $z - z_0 = 0$  denotes an approximate geometrical position 8 m off the chip edge. (a) Axial scans of a  $-20$  dB reflector as test sample placed at various depth positions  $z - z_0$ , showing a signal decay of  $3.3$  dB / mm. The black broken line is the spatial autocorrelation function of the light source with a  $10$  dB coherence length of  $l_c = 2 \times 6$  mm in vacuum. The position  $1$  mm coincides with the focus of the scan lens. The black dotted line represents the influence of defocusing on the reflected power coupled back into the on-chip waveguides. The sample is placed at distances from  $1$  mm to  $10$  mm within the scanning range, and the resulting scans are superimposed. For each curve, 100 subsequent scans are averaged. The measurement sensitivity is  $-64$  dB for objects placed in a region  $0.5 \text{ mm} \leq z - z_0 \leq 2 \text{ mm}$ . (b,c,d) Three-dimensional C-scans of biological and non-biological objects. The images are averages of 100 scans. (b) shows a piece of pumice, (c) a part of a decayed leaf of cornus sanguinea, and (d) a cross section of a reel of tape.

OCT<sub>int</sub> setup, aberrations caused by the use of a standard ball lens lead to suboptimal coupling. The limiting factors for both systems are coupling losses and on-chip backscatter. The OCT<sub>int</sub> exhibits a measured dynamic range of  $53$  dB, limited by the RIN contribution from the strong chip edge reflection. The dynamic range of the OCT<sub>ext</sub> is  $60$  dB, limited by the RIN contribution from a fully reflecting object.

We believe that our miniaturized OCT systems are suitable for a wide range of both medical and technical applications, including also advanced schemes such as Doppler OCT [21], optical coherence elastography (OCE) [22], or photo-thermal OCT [23]. By combining silicon photonic OCT engines with chip-scale swept-source lasers [24], fully integrated OCT systems come within reach. We report on a first proof-of-concept demonstration, with vast potential for improving the performance: Polymer microlenses, as used in OCT<sub>ext</sub>, could be used for the OCT<sub>int</sub> system as well, enhancing power coupling and reducing chip-edge reflections. Thus, a higher dynamic range and an improved sensitivity could be achieved with this system. For OCT<sub>ext</sub>, the effects of on-chip backscatter can be significantly improved by optimized fabrication processes and device design. In both cases, sensitivities better than  $-90$  dB can be achieved based on technological and design improvements. Moreover, we believe that compact and highly integrated OCT systems with tens or even hundreds of parallel spatial sensors will open completely new application spaces and create attractive market opportunities.

## Acknowledgments

This work was financed by Baden-Württemberg Stiftung gGmbH, by the European Research Council (ERC Starting Grant ‘EnTeraPIC’, number 280145), and by the Alfried Krupp von Bohlen und Halbach Foundation. We acknowledge support by the Karlsruhe School of Optics & Photonics (KSOP), by the Helmholtz International Research School for Teratronics (HIRST), by the Karlsruhe Nano-Micro Facility (KNMF), and by Deutsche Forschungsgemeinschaft and Open Access Publishing Fund of Karlsruhe Institute of Technology. Our chips were fabricated using the *OpSIS* service, through IME A\*STAR in Singapore, making use of design elements in the *OpSIS OI25A* PDK. The C-scans in Fig. 5(b,c,d) were visualized using the software *Vaa3D* [25–27].